



Corotating Interaction Regions during Solar Cycle 24: A Study on Characteristics and Geoeffectiveness

Rajkumar Hajra¹ · Jibin V. Sunny¹

Received: 12 August 2021 / Accepted: 2 February 2022
© The Author(s), under exclusive licence to Springer Nature B.V. 2022

Abstract

Corotating interaction regions (CIRs) form in the interaction region between the solar-wind high-speed streams and slow streams, leading to compressed plasma and magnetic fields. Using solar-wind measurements upstream of Earth, we identified 290 CIRs encountered by Earth during January 2008 through December 2019 (Solar Cycle 24). The occurrence rate is the maximum during the solar-cycle descending phase ($\approx 33 \text{ year}^{-1}$), followed by occurrences during solar minimum ($\approx 24 \text{ year}^{-1}$), the ascending phase ($\approx 22 \text{ year}^{-1}$), and solar maximum ($\approx 11 \text{ year}^{-1}$). At 1 AU, CIRs are found to be large-scale interplanetary structures with an average (median) duration of ≈ 26 hours (≈ 24 hours) and radial extent of ≈ 0.31 AU (≈ 0.27 AU). CIRs are characterized by average (median) plasma density of $\approx 29 \text{ cm}^{-3}$ ($\approx 26 \text{ cm}^{-3}$), ram pressure of ≈ 11 nPa (≈ 9 nPa), temperature of $\approx 5 \times 10^5$ K ($\approx 4 \times 10^5$ K), and magnetic-field magnitude of ≈ 15 nT (≈ 14 nT). The CIR characteristic features exhibit no clear solar-cycle phase dependence. About 30% of the CIRs are found to be geoeffective, causing geomagnetic storms with the peak SYM-H ≤ -50 nT; 25% caused moderate storms ($-50 \text{ nT} \geq \text{SYM-H} > -100$ nT), and 5% caused intense storms ($\text{SYM-H} \leq -100$ nT). The geoeffectiveness is found to decrease with the decreasing solar flux. CIRs during equinoxes are found to be more geoeffective compared to those during solstices. On average, SYM-H is strongly associated with the CIR plasma characteristic parameters (anti-correlation coefficient $r = -0.65$ to -0.89), while the association is weaker for the AE-index ($r = 0.41$ to 0.67).

Keywords Coronal Holes · Magnetic fields, Interplanetary · Magnetic Reconnection · Magnetosphere, Geomagnetic Disturbances · Solar Cycle · Solar Wind

1. Introduction

A corotating interaction region (CIR) is a compressed solar-wind plasma and magnetic-field region, forming between a slow ($\approx 300\text{--}450 \text{ km s}^{-1}$) solar-wind and a high-speed

✉ R. Hajra
rajkumarhajra@yahoo.co.in

J.V. Sunny
jibinsunny@gmail.com

¹ Indian Institute of Technology Indore, Simrol, Indore 453552, India

($\approx 500\text{--}800\text{ km s}^{-1}$) stream (HSS) emanated from a coronal hole on the Sun (Belcher and Davis, 1971; Siscoe, 1972; Krieger, Timothy, and Roelof, 1973; Smith and Wolfe, 1976; Pizzo, 1978). As coronal holes are generally long-lived structures on the rotating Sun, an HSS and the resultant CIR “corotate” with the Sun. Thus, they can be identified in interplanetary space more than once at an interval of ≈ 27 days, which is the solar differential rotation period at the solar Equator to mid-latitude regions (Snyder, Neugebauer, and Rao, 1963; Sheeley et al., 1977).

With varying heliocentric distance, the shape, size, and characteristics of a CIR change significantly (see Richardson, 2018, for an excellent review on this topic). CIR observations in the inner heliosphere have been made by the *Helios* 1 and 2, the *Pioneer Venus Orbiter*, the *Parker Solar Probe*, and the *Solar Orbiter* spacecraft (Richter and Luttrell, 1986; Jian, 2008; Jian et al., 2008a,b; Allen et al., 2020, 2021, and references therein). Near-Earth CIRs have been studied by several spacecraft, including the *Interplanetary Monitoring Platform* (IMP), *Geotail*, *Advanced Composition Explorer* (ACE), and *Wind* (Belcher and Davis, 1971; Tsurutani et al., 1995, 2006; Jian et al., 2006; Echer et al., 2011; Grandin, Aikio, and Kozlovsky, 2019; Nakagawa, Nozawa, and Shinbori, 2019; Hajra, Tsurutani, and Lakhina, 2020, and references therein). CIR studies in the outer heliosphere have used observations made by *Pioneer* 10 and 11, *Voyager* 1 and 2, and the *Rosetta* spacecraft (Gosling, Hundhausen, and Bame, 1976; Hundhausen and Gosling, 1976; Smith and Wolfe, 1976; Burlaga et al., 1984; Gazis et al., 1999; Jian et al., 2011; Hajra et al., 2018; Hajra, 2021a, and references therein). Based on these studies, it is inferred that the radial-velocity transition between the slow and fast streams steepens, and the plasma and magnetic-field compression along the CIR interface increases and becomes sharper with increasing radial distance. As a consequence, fast-forward and fast-reverse shocks form at the leading and trailing edges of a CIR, respectively, beyond ≈ 2 AU from the Sun (Gosling, Hundhausen, and Bame, 1976; Smith and Wolfe, 1976). At ≈ 1 AU, a CIR is typically characterized by gradually enhanced plasma density and magnetic-field magnitude and only rarely bounded by fast forward and reverse shocks (Belcher and Davis, 1971; Tsurutani et al., 1995; Jian et al., 2006).

Coronal-hole emanated HSSs are characterized by Alfvén wave trains (Tsurutani et al., 2006) that are strongly compressed within the CIRs. The southward component of the Alfvén waves reconnects with the northward (dayside) geomagnetic fields (Dungey, 1961). Thus, the CIR/HSS can largely affect the magnetosphere–ionosphere–thermosphere system of the Earth. This is generally called their “geoeffectiveness”. The major CIR/HSS impacts include: i) a rapid loss of relativistic (MeV) electrons in the Earth’s outer radiation belt due to magnetospheric compression by the ram-pressure enhancement during the CIR (Tsurutani et al., 2016a), followed by an electron acceleration during the following HSS (Hajra et al., 2014a, 2015a,b; Tsurutani et al., 2016b; Hajra and Tsurutani, 2018; Hajra, 2021b); ii) an enhancement of the ring currents in the inner magnetosphere leading to recurrent geomagnetic storms of moderate intensity (Tsurutani et al., 1995, 2006; Alves, Echer, and Gonzalez, 2006; Chi et al., 2018); iii) initiation of high-intensity long-duration continuous auroral electrojet (AE) activities (HILDCAAs: Tsurutani and Gonzalez, 1987; Hajra et al., 2013); iv) expansion and heating of the topside ionosphere (Hajra et al., 2017); and v) enhancements in thermospheric temperature and density (e.g. Lei et al., 2011; Gardner et al., 2012, and references therein).

While the CIR characteristics and impacts on Earth are well-explored topics, further statistical studies are required for a deeper understanding of the events and their impacts. Here we will present a compact study on both the characteristics and impacts of CIRs. The aim of the present work is to develop an updated catalog of all CIRs encountered by Earth during the most recently completed Solar Cycle 24 from January 2008 through December

2019. The catalog can be utilized by the space-weather research community for various research, modeling, and space-mission planning. Using all available solar-wind plasma and magnetic-field measurements upstream of the Earth, the general plasma and magnetic field characteristic features of the CIRs will be identified. These can be used as the typical CIR features for modeling purpose. It can be noted that most of the previous works used spacecraft in-situ solar-wind measurements, which are far from the Earth. In contrast, we will use the solar-wind plasma and magnetic-field measurements shifted to the Earth's bow-shock nose, considering the solar-wind propagation time from the spacecraft to the bow shock. These shifted data are more suitable for studying the near-Earth CIR characteristics and directly comparing them with the magnetospheric response. The geoeffectiveness of the CIRs causing geomagnetic storms will be studied using geomagnetic measurements. The relationships of the CIR characteristics with geomagnetic indices will also be explored. This study will hopefully enhance the predictive capacity of CIRs and the geomagnetic activity related to CIRs.

2. Database and Method of Analysis

CIRs are identified using high-resolution (one-minute) solar-wind plasma and interplanetary magnetic-field (IMF) data collected from NASA's OMNIWeb (omniweb.gsfc.nasa.gov/). These are observations made by the ACE, *Wind*, IMP 8, and *Geotail* spacecraft upstream of the Earth, which are shifted in time to take into account the arrival time of the solar wind to the Earth's bow-shock nose. The time-shifting is important for a direct comparison of the solar-wind variations with their geomagnetic impacts. In addition, the multi-spacecraft-based OMNI database can give complete and reliable statistics of CIRs encountered by Earth than any single spacecraft observation reported previously. The IMF measurements are in the geocentric solar magnetospheric (GSM) coordinate system, where the x -axis is directed towards the Sun and the y -axis is in the $\hat{\Omega} \times \hat{x}/|\hat{\Omega} \times \hat{x}|$ direction, $\hat{\Omega}$ is aligned with the magnetic south-pole axis of the Earth. The z -axis completes a right-hand system.

CIRs are identified manually as follows: First, from the temporal variation of the solar-wind plasma speed [V_{sw}], streams with $V_{sw} > 500 \text{ km s}^{-1}$ are determined as "potential" HSSs. Second, the solar sources of the streams are identified by exploring the solar coronal images (at the wavelength of 193 \AA) taken by the *Atmospheric Imaging Assembly* (AIA) instrument onboard NASA's *Solar Dynamics Observatory* (SDO: sdo.gsfc.nasa.gov/). Properties of the coronal holes, such as location on the Sun and magnetic polarity, were determined from the solar synoptic maps available at the Space Weather Prediction Center of National Oceanic and Atmospheric Administration (NOAA: www.swpc.noaa.gov/). The streams, depending on their speed between ≈ 500 and 800 km s^{-1} , can travel from the Sun to 1 AU in ≈ 2.0 – 3.5 days. If a coronal hole is identified (in the SDO/AIA images) within ≈ 2 – 3 days preceding the potential HSS identification at 1 AU, the stream is confirmed as a coronal-hole emanated-HSS. Third, for the confirmed HSS cases, the solar-wind plasma with enhanced density [N_{sw}], ram-pressure [P_{sw}], and IMF magnitude [B_0] in the interaction region between a slow stream and an HSS is identified as a CIR event.

In this work, a CIR is defined to be geoeffective if it causes a geomagnetic storm with the SYM-H peak (minimum) $\leq -50 \text{ nT}$ (Gonzalez et al., 1994). During a geomagnetic storm, the westward ring current, encircling the Earth's magnetic Equator at an altitude of ≈ 2 – 7 Earth radii (R_{\oplus}), is enhanced due to injection of energetic (≈ 10 – 300 keV) particles (e.g. H^+ , He^{2+}) from the solar wind and acceleration of the terrestrial thermal ions (e.g. O^+) (Frank, 1967; Shelley, Johnson, and Sharp, 1972; Williams, 1987; Hamilton et al.,

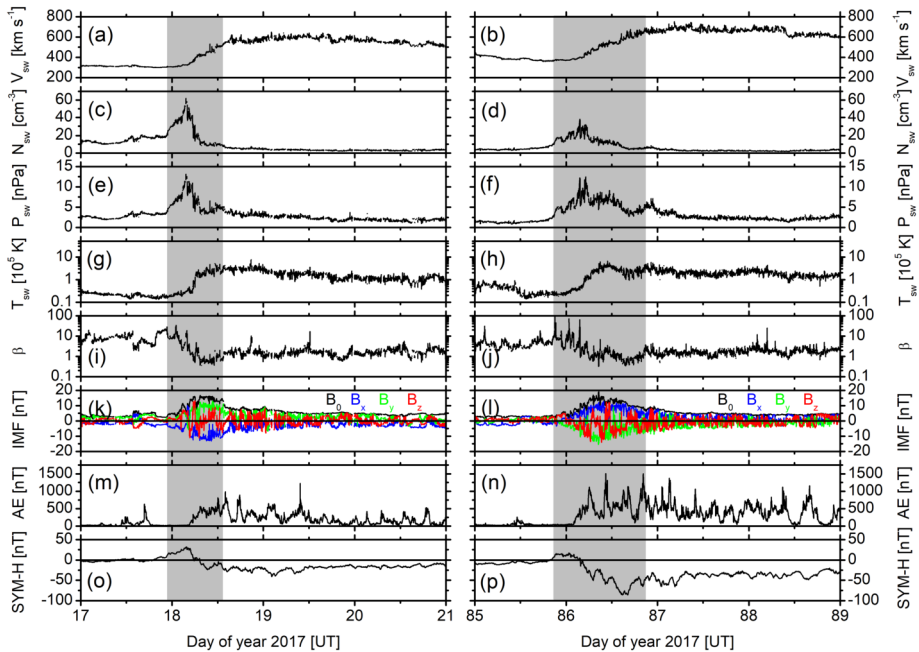


Figure 1 CIR events during 17–18 January 2017 (left) and 26–27 March 2017 (right). From top to bottom, the panels show (a–b) solar-wind plasma speed [V_{sw}], (c–d) plasma density [N_{sw}], (e–f) ram pressure [P_{sw}], (g–h) temperature [T_{sw}], (i–j) plasma- β , (k–l) IMF magnitude [B_0], and B_x -, B_y -, B_z -components, and geomagnetic indices (m–n) AE, and (o–p) SYM-H. The CIR intervals are marked by gray shading.

1988; Daglis et al., 1999). As a consequence, the low-latitude geomagnetic fields decrease, which is measured by the SYM-H index (Wanliss and Showalter, 2006; Iyemori et al., 2010). Following Gonzalez et al. (1994), storms are classified as moderate ($-50 \text{ nT} \geq \text{SYM-H} > -100 \text{ nT}$) or intense ($\text{SYM-H} \leq -100 \text{ nT}$) storms. We also studied the CIR impacts on the auroral ionosphere using the auroral electrojet (AE) index (Davis and Sugiura, 1966). The SYM-H and AE-indices (one-minute) are obtained from the World Data Center for Geomagnetism, Kyoto, Japan (wdc.kugi.kyoto-u.ac.jp/). Phases of the ≈ 11 -year solar cycle (Schwabe, 1844) are identified using the daily $F_{10.7}$ solar flux obtained from the Laboratory for Atmospheric and Space Physics (LASP) Interactive Solar Irradiance Data Center (lasp.colorado.edu/lisird/).

3. Results and Discussion

3.1. CIRs and their Geomagnetic Impacts: Case Studies

Figure 1 shows examples of two CIR events and their geomagnetic impacts during January 2017 and March 2017. The CIR intervals are marked by gray shadings.

The CIR event during January 2017 (Figure 1, left panels) resulted from the interaction between a slow solar-wind stream with a speed V_{sw} of $\approx 323 \text{ km s}^{-1}$ on Day 17 and an HSS with a peak V_{sw} of $\approx 640 \text{ km s}^{-1}$ identified on Day 19 (Figure 1a). The HSS was emanated from a solar equatorial coronal hole on Day 17 shown in Figure 2a. The coronal

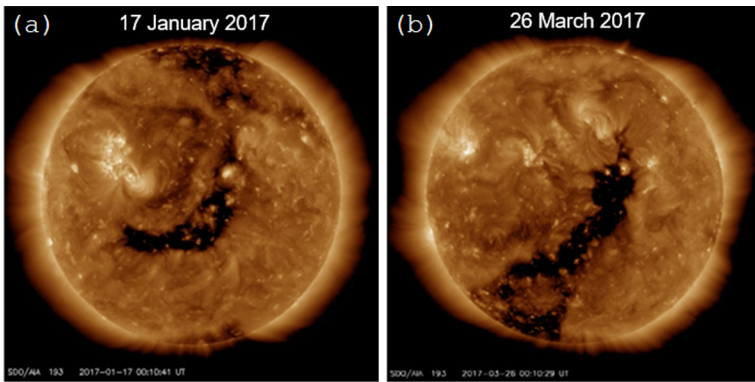


Figure 2 Solar images taken by the SDO/AIA instrument at the wavelength of 193 Å. The dark regions around the center of each image show the coronal holes. The coronal holes on 17 January (Day 17) and 26 March (Day 85) 2017 are the sources of HSSs identified on Days 19 and 87, respectively, shown in Figure 1.

hole had a “positive” magnetic polarity (i.e. magnetic field pointing away from the Sun). This is consistent with the anti-sunward IMF direction as evident from the negative B_x - and positive B_y -values during the HSS (Figure 1k). While there are no clear/sharp boundaries of the CIR, from the gradual increases in the IMF magnitude [B_0] (Figure 1k), plasma density [N_{sw}] (Figure 1c), and ram-pressure [P_{sw}] (Figure 1e), a CIR is identified from $\approx 22:52$ UT on Day 17 to $\approx 13:57$ UT on Day 18. Compared to the ambient solar wind, the CIR is a compressed plasma region, characterized by a peak B_0 of ≈ 16.8 nT, a peak N_{sw} of ≈ 62.0 cm $^{-3}$, and a peak P_{sw} of ≈ 13.2 nPa. The plasma- β (defined as the ratio of the plasma pressure to the magnetic pressure) decreased from ≈ 22.8 to ≈ 0.4 (Figure 1i). The plasma temperature [T_{sw}] exhibits a gradual increase during the CIR (Figure 1g), similar to the V_{sw} variation. Using the gradually increasing V_{sw} from ≈ 309 to ≈ 553 km s $^{-1}$ during the entire CIR interval, we estimated the radial extent of the CIR, as the “area under the V_{sw} curve”, to be ≈ 0.18 AU.

The CIR starting at $\approx 22:52$ UT on Day 17 is accompanied by a gradual increase in the geomagnetic SYM-H index to +32 nT at $\approx 03:47$ UT on Day 18 (Figure 1o). This is caused by compression of the magnetosphere by enhanced P_{sw} during the CIR. A negative excursion of SYM-H and an increase in AE are associated with a short-duration (\approx one hour) southward IMF component with a minimum B_z of -11 nT at $\approx 04:41$ UT on Day 18. During the entire CIR interval, the peak AE and the minimum SYM-H values of 815 nT and -24 nT, respectively, show that the CIR was not geoeffective enough to cause a magnetic storm.

The March 2017 CIR event (Figure 1, right panels) from $\approx 20:47$ UT on Day 85 to $\approx 20:42$ UT on Day 86 occurred in the intersection region between a low-speed stream with V_{sw} of ≈ 390 km s $^{-1}$ on Day 85 and an HSS with a peak V_{sw} of ≈ 726 km s $^{-1}$ on Day 87 (Figure 1b). The coronal hole on Day 85 emanating this HSS (Figure 2b) had a “negative” magnetic polarity (i.e. magnetic field pointing towards the Sun). This is consistent with the positive B_x - and negative B_y -components indicating a sunward IMF direction (Figure 1l) during the HSS. The radial extent of the CIR is estimated to be ≈ 0.25 AU. The CIR is characterized by the peak B_0 of ≈ 19.1 nT, N_{sw} of ≈ 38.1 cm $^{-3}$, P_{sw} of ≈ 12.5 nPa. While β decreased from ≈ 12.1 to ≈ 0.3 , T_{sw} exhibited a gradual increase as in V_{sw} during the CIR. The CIR is found to be geoeffective, causing a moderate magnetic storm with a peak SYM-H of -86 nT at $\approx 14:46$ UT on Day 86. The storm main phase exhibits a three-step develop-

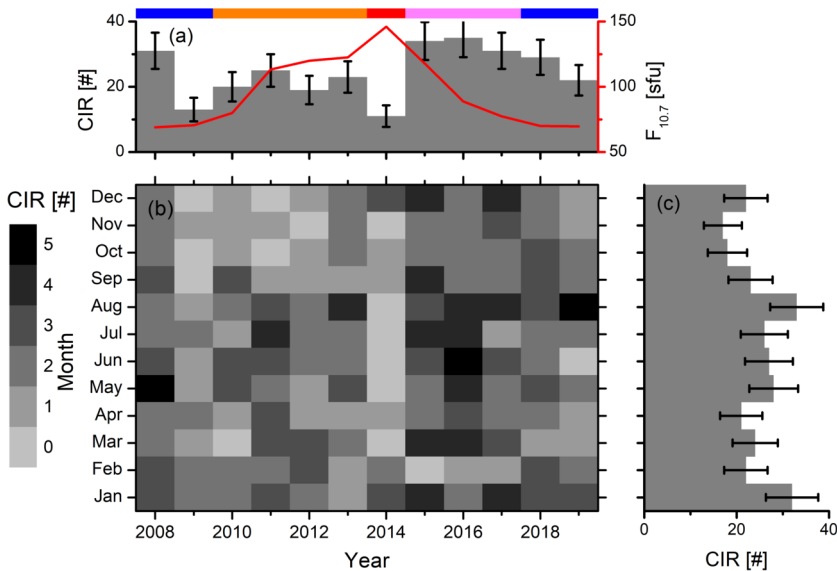


Figure 3 Seasonal and solar-cycle dependence of CIRs. (a) Yearly number of CIRs (histograms, the legend on the left) with Poisson counting-errors (vertical bars), and yearly mean $F_{10.7}$ solar flux (red, legend on the right), (b) year-month number of CIRs, values of different shading are given in legend on the left, (c) monthly number of CIRs with Poisson counting-error bars. The solar-cycle phases are shown by color-coded horizontal bars at the top, as the solar minimum (blue), the ascending phases (orange), the maximum (red), and the descending phase (pink).

ment, correlated with three episodes of southward IMFs with durations of ≈ 2.1 , ≈ 1.6 , and ≈ 3.0 hours and the minimum B_z of ≈ -13.6 , ≈ -14.1 , and ≈ -11.3 nT, respectively. They also triggered substorms with the peak AE of ≈ 1118 , ≈ 1505 , and ≈ 1038 nT, respectively, during the main phase.

3.2. Solar Cycle and Seasonal Variations of CIRs and Their Geoeffectiveness

Following the method described in Section 2, we identified a total of 290 CIRs from January 2008 to December 2019. The CIR events are listed in Appendix Table 3 and are shown as year-month numbers in Figure 3b. The superposed numbers of events in each year and each month are shown as histograms in Figures 3a and 3c, respectively, along with the associated Poisson counting-error bars. The most prominent features noted from Figure 3b are the largest population of events during the years 2015–2017 (yearly 34, 35, and 31 events, respectively) and the smallest occurrence during 2014 (only 11 events). From the yearly mean $F_{10.7}$ solar-flux variation (Figure 3a, red), the year 2014 corresponds to the maximum of Solar Cycle 24, while the years 2015–2017 are in the descending phase. The solar flux is expressed in the solar flux unit [sfu, where $1 \text{ sfu} = 10^{-22} \text{ W m}^{-2} \text{ Hz}^{-1}$].

Based on the $F_{10.7}$ solar-flux values, the entire period of study (from January 2008 to December 2019) is divided into: the solar minimum (years 2008–2009 and 2018–2019 with $F_{10.7}$ of ≈ 69 – 71 sfu), the ascending phase (years 2010–2013 with $F_{10.7}$ of ≈ 80 – 123 sfu), the maximum (the year 2014 with $F_{10.7}$ of ≈ 146 sfu), and the descending phase (years 2015–2017 with $F_{10.7}$ of ≈ 77 – 118 sfu) as shown by the horizontal color-coded bars in Figure 3a (top). The CIR occurrence rate is found to be the highest during the descending

Table 1 CIRs causing geomagnetic storms.

Storm type	Number	Percent
Moderate ($-50 \text{ nT} \geq \text{SYM-H} > -100 \text{ nT}$)	74	25
Intense ($\text{SYM-H} \leq -100 \text{ nT}$)	14	5
All ($\text{SYM-H} \leq -50 \text{ nT}$)	88	30

phase ($\approx 33 \text{ year}^{-1}$), followed by occurrences during the solar minimum ($\approx 24 \text{ year}^{-1}$), the ascending phase ($\approx 22 \text{ year}^{-1}$), and the solar maximum ($\approx 11 \text{ year}^{-1}$). Alves, Echer, and Gonzalez (2006) studied all near-Earth CIRs during 1964–2003 without exploring such solar-cycle dependence. Jian et al. (2006) studied the near-Earth CIRs encountered by the *Wind* and ACE spacecraft during 1995–2004 and reported only little variation in their annual numbers. Jian et al. (2019) surveyed all CIRs encountered by the *Solar Terrestrial Relations Observatory* (STEREO) spacecraft during 2007–2016, finding a larger number of events during the descending phase.

The above-mentioned solar-cycle dependence of CIRs can be explained as a result of varying coronal-hole size and location with the ≈ 11 -year solar cycle. Coronal holes are normally located near the polar regions of the Sun at solar maximum. However, the holes expand in size and move towards the Equator during the solar-cycle descending phase and the solar minimum (Burlaga et al., 1978; Sheeley and Harvey, 1981). HSSs emanated from the equatorial coronal holes and the consequent CIRs have a higher probability of encountering Earth in the ecliptic plane of the Sun. Thus, the near-Earth CIR occurrence rate is higher during the descending to minimum solar-cycle phases compared to the solar maximum and ascending phases (Richardson, Cliver, and Cane, 2000; Tsurutani et al., 2006).

As expected, the CIR distribution does not exhibit any seasonal dependence (Figure 3c). During the entire period of observation, the largest number of events (33) are recorded during August with a comparable number (32) during January and the smallest number (17) during November.

Among all the 290 CIR events identified in this work, only 88 (i.e. $\approx 30\%$ of the CIRs) caused geomagnetic storms with the SYM-H peak $\leq -50 \text{ nT}$ (Table 1). When separated on the basis of the peak SYM-H values, 25% of the CIRs caused moderate storms and 5% caused intense storms. None of the CIRs caused any super storms ($\text{SYM-H} \leq -250 \text{ nT}$). The results are consistent with Alves, Echer, and Gonzalez (2006), who reported that $\approx 33\%$ of all CIRs occurring during 1964–2003 were geoeffective, and only $\approx 2.5\%$ caused the intense storms. Chi et al. (2018) reported that $\approx 22\%$ and $\approx 3\%$ of all CIRs encountered by *Wind* or ACE during 1995–2016 resulted in the moderate and intense storms at Earth, respectively.

The seasonal and solar-cycle dependencies of the CIRs causing geomagnetic storms are shown in Figure 4. Figure 4b shows the percent of CIRs causing a geomagnetic storm during each month of each year of the entire period of study. Based on this data, the yearly and monthly superposed storm occurrences are shown by histograms in Figures 4a and 4c, respectively.

During the year 2014 (the solar maximum), $\approx 27\%$ of the 11 CIRs caused geomagnetic storms. During the years (2012–2013) preceding the solar maximum, CIRs occurring during the first half of the years are found to be more geoeffective compared to those occurring during the second half (Figure 4b). The reverse is true for the years (2015–2016) following the solar maximum when geoeffectiveness is higher during the second half of the years. This resulted in an overall semiannual variation of the geoeffectiveness, showing two peaks

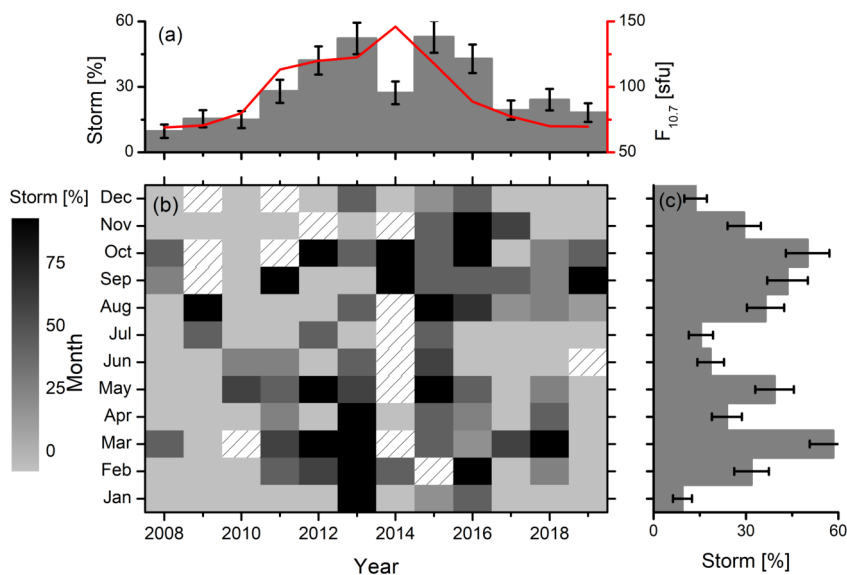


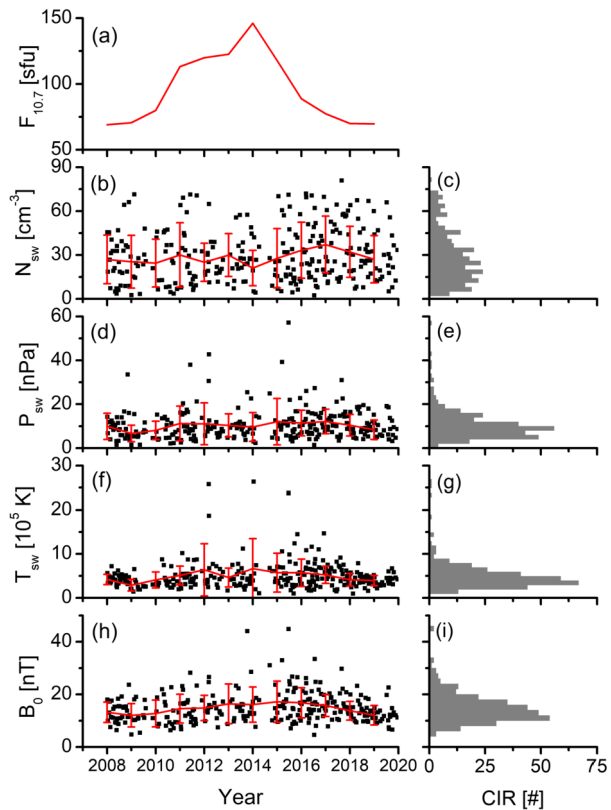
Figure 4 Geoeffectiveness of CIRs. (a) Yearly percentage of CIRs causing geomagnetic storms (histograms, legend on the left) with Poisson counting-errors (vertical bars), and yearly mean $F_{10.7}$ solar flux (red, the legend on the right), (b) year-month numbers of CIRs causing geomagnetic storms, values of different shading are given in legend on the left, hatching lines indicates intervals with no CIR, (c) monthly percentage of CIRs causing geomagnetic storms with Poisson, counting-error bars.

around March and October and minima around January and July (Figure 4c). Another interesting feature is that on both sides of the solar maximum, the geoeffectiveness decreases with the decreasing $F_{10.7}$ solar flux (Figure 4a). The yearly CIR geoeffectiveness exhibits a significant correlation (correlation coefficient $r = 0.66$) with the yearly mean $F_{10.7}$ solar flux.

The seasonal dependence of the CIR geoeffectiveness is consistent with the results reported by Richardson et al. (2006) and Zhang et al. (2008). The result depicts the well-known semi-annual variation of the geomagnetic activity (see Broun, 1848; Sabine, 1852; Baker et al., 1999; Cliver, Kamide, and Ling, 2000; Kanekal, Baker, and McPherron, 2010; Danilov, Krymskii, and Makarov, 2013; Lockwood et al., 2020; Marques de Souza Franco et al., 2021; Hajra, 2021b, and references therein). This is generally discussed in the context of three mechanisms, namely: i) the “axial effect” (Cortie, 1912), which is related to the Earth’s position in the heliosphere, ii) the “equinoctial effect” (Boller and Stolov, 1970), related to the relative angle of solar-wind incidence with respect to the Earth’s rotation axis, and iii) the “Russell–McPherron effect” (Russell and McPherron, 1973), related to the geometrical controls of IMFs. However, which of the mechanisms is dominating here is not known at present.

The correlation of the CIR geoeffectiveness with the solar flux is interesting. It may be related to an overall higher value of the solar-wind–magnetosphere coupling during the solar maximum, and its decreasing value with the decreasing solar flux (e.g. Hajra, 2021c, and references therein). This should be explored further. Another plausible reason for the enhanced CIR geoeffectiveness during the solar maximum could be the interaction of CIRs with the interplanetary coronal mass ejections (ICMEs), as suggested by Chi et al. (2018). ICMEs are the interplanetary remnants of the coronal mass ejections (CMEs: e.g. Illing and

Figure 5 Plasma properties during CIRs. **(a)** Yearly mean $F_{10.7}$ solar flux, **(b)** plasma density [N_{sw}] during CIRs, **(c)** histograms of N_{sw} , **(d)** ram pressure [P_{sw}] during CIRs, **(e)** histograms of P_{sw} , **(f)** temperature [T_{sw}] during CIRs, **(g)** histograms of T_{sw} , **(h)** IMF magnitude [B_0] during CIRs, **(i)** histograms of B_0 . In the left panels, red-solid lines show the yearly mean values, and vertical bars show the standard deviations from the mean.



Hundhausen, 1986), which can be rotated/modified when propagating through the interplanetary medium (e.g. Odstrčil and Pizzo, 1999; Yurchyshyn et al., 2007; Palmerio et al., 2018). The interplanetary medium is dominated by ICMEs during the solar-cycle maximum (e.g. Webb and Howard, 1994; Gopalswamy et al., 2004; Tsurutani et al., 2006; Obridko et al., 2012). Chi et al. (2018) reported a remarkably higher geoeffectiveness of the CIR–ICME combined structures than the isolated CIRs, which seems to be consistent with the present result.

3.3. Characteristics of CIRs and Relationship with Geomagnetic Indices

For each of the CIRs, we computed the characteristic plasma and IMF variations, that is the peak N_{sw} , P_{sw} , T_{sw} , B_0 during the CIRs, and duration and radial extent of the CIRs. The results are shown in Figures 5 and 6 and summarized in Table 2. In Table 2, we also list the average values of the solar-wind parameters based on the upstream solar-wind measurements for the period from 1963 through 2021. This is referred to as the “average” solar wind in Table 2 and is used to compare the plasma/field compression during the CIRs. In Figures 5 and 6, the top Panel a shows the yearly mean $F_{10.7}$ solar flux. This is followed by characteristic parameters during each of the CIR events (the black points) with the superposed yearly mean (the red points connected by lines) and standard (1- σ) deviations (bars) in the left panels. The right panels show distributions of the CIRs for different ranges of the characteristic parameters in the form of histograms.

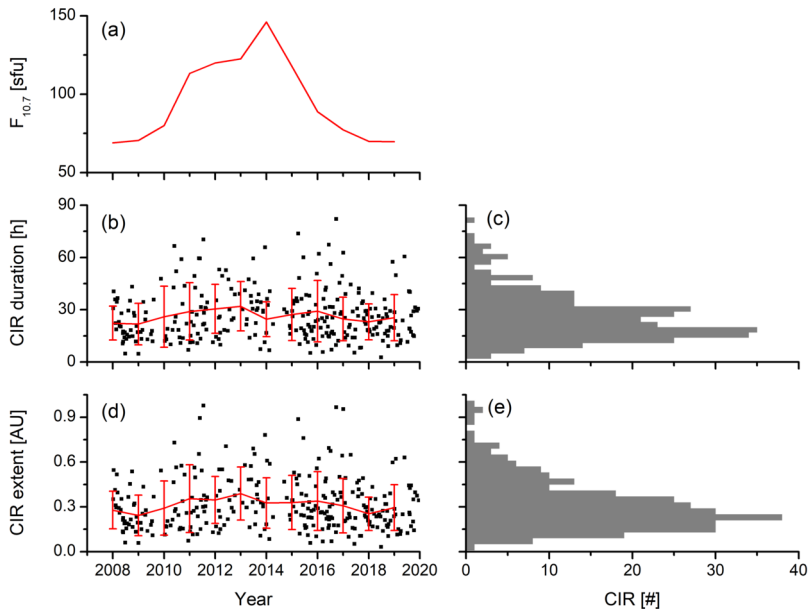


Figure 6 Extents of CIRs. **(a)** Yearly mean $F_{10.7}$ solar flux, **(b)** duration of CIRs, **(c)** histograms of CIR duration, **(d)** extent of CIRs, **(e)** histograms of CIR extents. In the *left panels*, *red-solid lines* show the yearly mean values, and *vertical bars* show the standard deviations from the mean.

Table 2 Average characteristics and geomagnetic impacts of CIRs.

Parameter	CIR				“Average” solar wind	
	Minimum	Maximum	Median	Mean \pm SD ^a	Median	Mean \pm SD ^a
N_{sw} [cm ⁻³]	2.4	81.0	25.7	29.3 \pm 18.0	5.2	6.7 \pm 5.4
P_{sw} [nPa]	1.4	57.2	9.0	10.5 \pm 6.7	1.8	2.3 \pm 1.9
T_{sw} [10 ⁵ K]	0.97	26.35	4.26	4.91 \pm 3.13	0.74	1.02 \pm 0.98
B_0 [nT]	4.6	44.9	13.8	14.8 \pm 5.6	4.8	5.5 \pm 3.0
Duration [hours]	2.75	82.10	23.58	26.47 \pm 14.09	–	–
Extent [AU]	0.03	0.98	0.27	0.31 \pm 0.17	–	–
AE [nT]	57	2698	1072	1137 \pm 457	–	–
SYM-H [nT]	–223	1	–35	–42 \pm 31	–	–

^aSD == standard deviation.

The yearly mean CIR characteristic parameters exhibit no obvious relationship with the solar $F_{10.7}$ flux variation (Figures 5 and 6). The CIR characteristics exhibit a large variation from event to event. This is reflected in the large 1- σ deviations from the yearly mean values. The deviations are ≈ 61 – 64% for the plasma parameters, $\approx 38\%$ for the IMF B_0 , and for the duration and extent, the deviations are ≈ 53 – 55% of their corresponding mean values (Table 2).

From the distribution of the characteristic parameters for 290 CIR events (Figures 5 and 6, right panels), the average and median CIR characteristics are listed in Table 2. CIRs

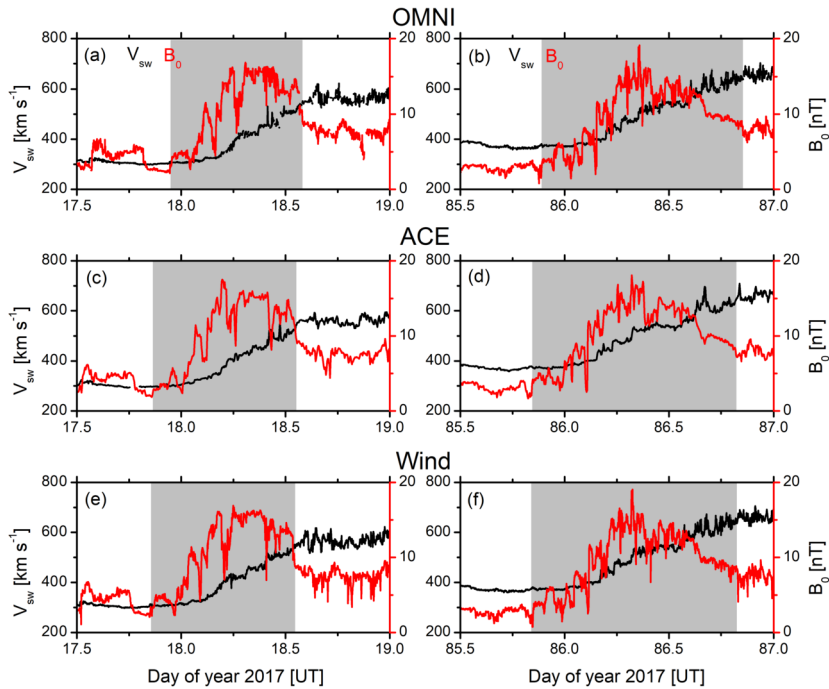


Figure 7 CIR events during 17–18 January 2017 (left) and 26–27 March 2017 (right). Each of the panels shows solar-wind plasma speed [V_{sw}] (black, axis on the left), and IMF magnitude [B_0] (red, axis on the right). From top to bottom, panels show data collected from OMNI, ACE, and Wind, respectively. The CIR intervals are marked by gray shading.

are found to be large-scale interplanetary events/structures, with an average duration of the order of a day (Figure 6b–c, Table 2) and the radial extent of ≈ 0.3 AU (Figure 6d–e, Table 2). Interestingly, the CIR plasma parameters are ≈ 4 – 6 times, and the IMF magnitude is \approx three times, the “average” solar-wind parameters (Table 2). For comparison, the average CIR B_0 -peak reported by Alves, Echer, and Gonzalez (2006), Jian et al. (2006), and Jian et al. (2019) are ≈ 14 nT, ≈ 15 nT, and ≈ 13 nT, respectively. The values are approximately identical to the present estimation ($\approx 15 \pm 6$ nT). It may be noted that the CIR N_{sw} - and T_{sw} -values reported in this work were not reported in the previous works.

However, the average CIR duration reported by Jian et al. (2006, 2019) is ≈ 1.5 times the CIR duration obtained in this work. There can be several possible reasons behind this inconsistency. The present computations are based on the solar-wind data propagated to the Earth’s bow-shock nose (OMNI), while the Jian et al. (2006, 2019) results are based on the Wind, ACE, and STEREO spacecraft in-situ measurements. Perhaps the act of time shifting from slow to fast solar wind might have deformed the shape of the structure in the OMNI dataset slightly. To verify this possibility, we have studied a few CIR events using OMNI, ACE, and Wind data. Figure 7 shows variations of solar-wind plasma speed [V_{sw}] and IMF magnitude [B_0] collected from OMNI, ACE, and Wind for the CIR events shown in Figure 1. The CIR intervals for each observation are shown by gray shadings. For the January 2017 event (left panel), the CIR interval observed by OMNI is ≈ 1.4 hours shorter than the same observed by ACE and Wind. For the March 2017 event (right panel), the OMNI CIR duration is only ≈ 0.5 hours shorter than observed by ACE and Wind. While

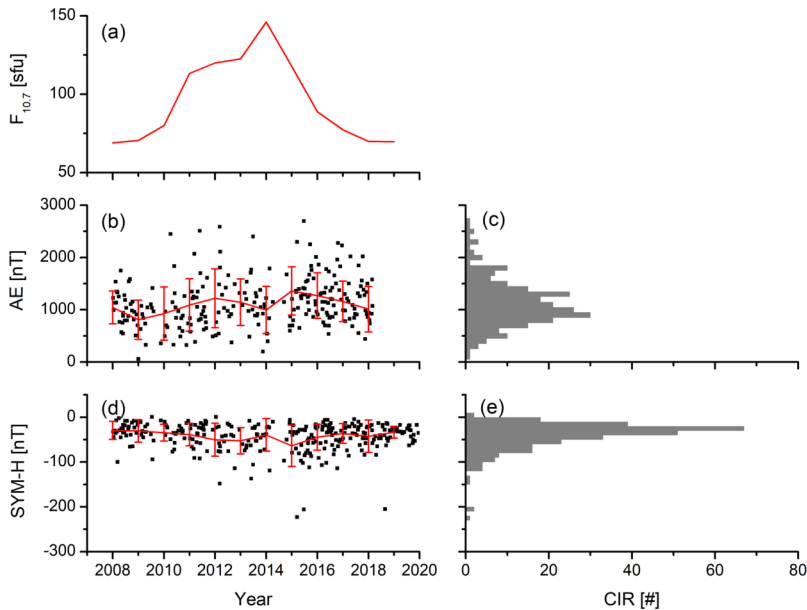


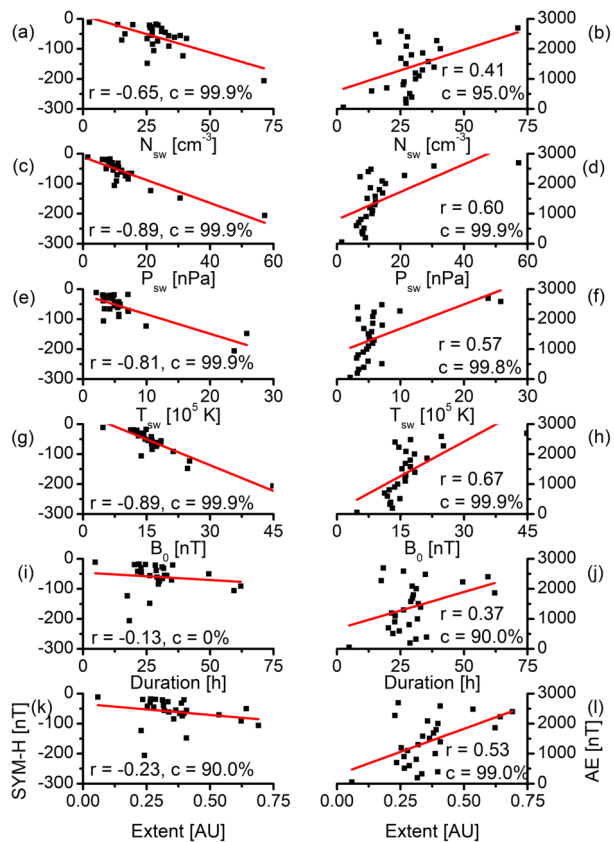
Figure 8 Geomagnetic impacts of CIRs. (a) Yearly mean $F_{10.7}$ solar flux, (b) the maximum AE values during CIRs, (c) histograms of AE, (d) the minimum SYM-H values during CIRs, (e) histograms of SYM-H. In the left panels, red-solid lines show the yearly mean values, and vertical bars show the standard deviations from the mean.

the differences of the CIR duration in OMNI data and the spacecraft in-situ observations seem to be small in these examples, the OMNI time-shifting is probably compressing the CIR structure slightly in some cases. In other words, the perceived shortening in the CIR duration from L_1 to the nose of the bow shock (from the OMNI data set) may be an artifact of the propagation scheme used in OMNI not being well suited for these types of sudden changes in the solar wind. The algorithms used by OMNI to compute the propagation time do not take into account the dynamics at the CIR interface. So the propagation time of the high-speed region of the CIR might be faster than reality. Another possibility may be related to the uncertainty in defining the CIR boundary. As only a few of CIRs at 1 AU are bounded by a shock pair at the leading and trailing edges, the CIR boundaries cannot be defined with high precision for most of the CIRs, leading to uncertainty in the computation of the CIR duration.

Figure 8 shows the solar-cycle variations of the geomagnetic AE and SYM-H indices during the CIR events. Overall, the AE peaks and the SYM-H minima are larger during the descending phase compared to the ascending phase of the solar cycle. From the distribution of AE (Figure 8c) and SYM-H (Figure 8e), and the average and median values listed in Table 2, most of the CIRs are found to be associated with the low levels of geomagnetic activity, consistent with Alves, Echer, and Gonzalez (2006).

Figure 9 shows the regression analysis of the SYM-H minima and the AE-peaks with the CIR characteristic parameters, namely, the peak values of N_{sw} , P_{sw} , T_{sw} , IMF B_0 during the CIRs, and the CIR durations and radial extents. The correlation coefficient of the SYM-H index with the solar-wind plasma and magnetic-field parameters varies between -0.65 and -0.89 ; the SYM-H peak correlation is exhibited with P_{sw} and B_0 . For the AE-index, the correlation coefficient varies between 0.41 and 0.67 , and the AE peak correlation is exhibited

Figure 9 Average geomagnetic activity vs. CIR characteristics. Variations of the SYM-H (left panels) and AE-indices (right panels) with N_{sw} (a–b), P_{sw} (c–d), T_{sw} (e–f), B_0 (g–h), CIR duration (i–j), and CIR extent (k–l). The linear regression lines, regression coefficients [r], and confidence levels [c] of the regression coefficients are shown in each panel.



with B_0 . Thus, the IMF B_0 is found to be the most important solar-wind parameter for the prediction of the geomagnetic activity during CIRs. Overall lower correlation of the AE-index, compared to the SYM-H index, with the solar-wind parameters is related to varying physical processes occurring in different regions of the inner magnetosphere and ionosphere. The AE-index, related to the auroral ionospheric currents flowing at ≈ 100 km altitude, is strongly controlled by the ionospheric conductivity (Wang and Lühr, 2007; Tanskanen et al., 2011). On the other hand, the ring current (presented by SYM-H) variability is directly impacted by the solar-wind dynamics (see Daglis et al., 1999, and references therein).

The CIR duration and radial extent seem to exhibit no relationship with the ring-current intensity (Figure 9i, k). However, the CIRs with larger extent seem to be associated with the increased intensity of the auroral activity (Figure 9l). This should be explored further to understand the underlying physical processes. While Alves, Echer, and Gonzalez (2006) and Zhang et al. (2008) explored the relationships of the geomagnetic-storm strength with a few solar-wind and IMF parameters during CIRs, the present correlation analyses involve additional CIR characteristic parameters such as plasma density, ram pressure, temperature, CIR duration and radial extent, and the geomagnetic auroral electrojet variation for the first time. These present a more complete study and are important for developing predictive models of the CIR geoeffectiveness based on solar-wind measurements.

4. Summary and Conclusion

A database of 290 CIRs encountered by Earth during January 2008 through December 2019 (Solar Cycle 24) is developed using upstream solar-wind plasma and IMF measurements shifted to the Earth's bow-shock nose. The CIR database is provided in Appendix Table 3 for the research community. The solar-wind measurements along with the geomagnetic indices are utilized for a detailed quantitative study on the CIR characteristics and impacts. The main findings of this work may be summarized as follows:

- i) While CIRs can occur during any phase of a solar cycle, the occurrence rate is significantly higher during the descending phase ($\approx 33 \text{ year}^{-1}$) compared to the solar minimum ($\approx 24 \text{ year}^{-1}$), the ascending phase ($\approx 22 \text{ year}^{-1}$), and solar maximum ($\approx 11 \text{ year}^{-1}$) (Figure 3).
- ii) On average, CIRs are characterized by the peak plasma density of $\approx 29 \text{ cm}^{-3}$, ram pressure of $\approx 11 \text{ nPa}$, temperature of $\approx 5 \times 10^5 \text{ K}$, and magnetic-field magnitude of $\approx 15 \text{ nT}$. The solar-wind plasma parameters (density, temperature, ram pressure) during the CIRs are ≈ 4 – 6 times enhanced compared to their values for the “average” solar wind, while the compression is \approx three times in the magnetic-field magnitude (Figure 5, Table 2). The CIR plasma and magnetic-field characteristics do not exhibit any prominent solar-cycle dependence.
- iii) CIRs are found to be a large-scale interplanetary structure, with an average duration of the order of a day, and an average radial extent of $\approx 0.31 \text{ AU}$ (Figure 6, Table 2).
- iv) Only 30% of all CIRs under this study are found to be geoeffective in causing the geomagnetic storms with the SYM-H peak $\leq -50 \text{ nT}$ (Table 1). While the CIR occurrence peaks during the solar-cycle descending phase (Figure 3a), the geoeffectiveness of CIR decreases with decreasing solar flux (Figure 4a). The latter result is related to an overall decrease in the geoeffectiveness of the solar wind and solar-wind–magnetosphere coupling with the decreasing solar flux. The enhanced CIR geoeffectiveness during solar maximum may be plausibly associated with the CIR–ICME interactions.
- v) Geoeffectiveness of CIRs exhibits a clear semi-annual variation with two equinoctial peaks and the solstice minima (Figure 4c). This result is attributed to the semi-annual variation of the solar-wind–magnetosphere coupling efficiency.
- vi) The CIR plasma and magnetic-field characteristics seem to have significant control on the geomagnetic impacts of CIR as evident from the high correlation between the solar-wind parameters and the geomagnetic indices (Figure 9). The overall higher correlation of the ring-current index SYM-H compared to the auroral ionospheric index AE is associated with varying physical processes occurring in different parts of the inner magnetosphere and ionosphere.

The present investigation of the CIR characteristics is based on the solar-wind measurements propagated to the Earth's bow-shock nose. However, the large-scale CIR interplanetary structures expand radially (with the heliocentric distance) and become well-developed as they expand. The fast-forward and fast-reverse shocks form at the leading and trailing edges of a CIR at large heliocentric distances through the non-linear steepening of the waves. It will be interesting to study how the CIR radial extent varies depending on the heliocentric distance. A future study can be done on this using multi-spacecraft data analysis.

Appendix

Table 3 presents a catalog of all CIRs identified from January 2008 through December 2019. The approximate start and end times are given as the day of the year. The table is available in the Electronic Supplementary Material.

Table 3 Catalog of all CIRs under this study. The approximate start and end times at Earth are given as the day of the year [DOY].

Year	Start [DOY]	End [DOY]
2008	5.0	6.3
2008	12.2	13.9
2008	31.5	33.0
2008	41.1	42.1
2008	49.2	50.0
2008	58.6	60.1
2008	68.3	69.8
2008	86.1	87.0
2008	95.3	96.1
2008	113.9	114.7
2008	124.0	125.2
2008	141.7	142.2
2008	144.6	145.3
2008	148.9	149.7
2008	166.6	167.2
2008	171.8	172.5
2008	177.7	177.9
2008	194.0	194.5
2008	204.3	205.0
2008	222.0	223.2
2008	231.0	231.6
2008	247.2	248.6
2008	258.8	259.5
2008	274.7	276.5
2008	285.2	285.9
2008	302.2	303.4
2008	311.9	313.0
2008	330.0	330.5
2008	340.5	341.4
2008	357.3	358.0
2009	1.0	1.2
2009	30.9	31.6
2009	45.1	45.6
2009	57.9	58.7
2009	71.0	72.4
2009	98.7	99.7
2009	106.0	107.2
2009	129.0	129.6
2009	179.7	180.4
2009	194.4	195.1
2009	203.0	203.5
2009	217.4	218.9
2009	323.7	325.7

Table 3 (Continued.)

Year	Start [DOY]	End [DOY]
2010	11.3	11.8
2010	20.4	21.0
2010	33.6	34.1
2010	49.2	50.0
2010	95.3	95.8
2010	122.2	123.0
2010	138.2	139.9
2010	148.1	150.9
2010	154.6	155.6
2010	166.1	167.2
2010	176.4	178.5
2010	207.7	208.5
2010	222.6	223.2
2010	235.8	236.3
2010	248.7	251.1
2010	266.0	267.4
2010	270.9	271.4
2010	295.4	297.2
2010	322.0	322.9
2010	346.6	346.9
2011	6.8	7.3
2011	13.4	14.0
2011	18.6	19.6
2011	35.1	36.3
2011	45.7	46.1
2011	60.1	61.0
2011	69.3	71.3
2011	80.8	82.5
2011	101.7	102.8
2011	109.9	110.3
2011	119.6	120.3
2011	134.6	137.1
2011	146.6	149.1
2011	155.9	156.4
2011	164.5	165.9
2011	173.1	174.7
2011	192.4	193.3
2011	198.7	201.6
2011	205.8	207.0
2011	211.1	212.0
2011	225.8	227.1
2011	234.8	236.1
2011	240.7	241.4
2011	252.5	254.0

Table 3 (Continued.)

Year	Start [DOY]	End [DOY]
2011	332.9	333.4
2012	12.7	13.3
2012	15.7	17.2
2012	49.9	50.4
2012	53.1	54.1
2012	57.9	60.1
2012	68.5	69.6
2012	72.4	73.1
2012	75.5	75.9
2012	102.1	104.1
2012	129.7	130.5
2012	154.6	156.8
2012	181.9	182.7
2012	190.4	192.3
2012	205.0	206.3
2012	231.2	232.9
2012	237.3	238.3
2012	263.5	264.6
2012	282.5	284.2
2012	352.1	353.7
2013	25.7	26.9
2013	59.6	61.3
2013	79.4	80.3
2013	87.8	88.9
2013	113.2	115.2
2013	126.2	126.8
2013	144.8	146.3
2013	151.7	153.1
2013	171.1	172.4
2013	178.6	181.1
2013	198.8	200.7
2013	206.5	207.2
2013	216.3	217.2
2013	227.2	228.4
2013	232.8	234.3
2013	242.3	243.5
2013	255.5	257.1
2013	281.8	282.1
2013	287.1	288.6
2013	319.6	320.8
2013	341.9	342.4
2013	347.6	350.3
2014	1.3	2.0
2014	12.8	14.3

Table 3 (Continued.)

Year	Start [DOY]	End [DOY]
2014	21.0	22.3
2014	41.7	42.0
2014	50.1	51.8
2014	95.9	96.9
2014	255.7	256.9
2014	293.1	294.3
2014	335.2	336.1
2014	340.2	340.9
2014	345.9	346.8
2015	4.2	5.5
2015	10.3	11.4
2015	21.0	22.4
2015	31.8	33.2
2015	60.9	61.6
2015	64.9	66.5
2015	76.2	77.6
2015	90.4	93.4
2015	104.3	106.3
2015	110.8	111.2
2015	132.7	133.5
2015	138.1	139.6
2015	158.4	159.5
2015	163.6	166.1
2015	173.7	174.5
2015	185.5	186.2
2015	191.8	192.3
2015	203.7	205.3
2015	208.0	208.6
2015	227.4	227.8
2015	230.8	232.0
2015	234.8	235.7
2015	246.5	247.7
2015	251.1	252.7
2015	257.0	257.8
2015	263.2	263.5
2015	280.1	280.9
2015	285.3	286.1
2015	307.0	307.5
2015	313.5	314.4
2015	340.8	341.8
2015	343.6	345.0
2015	348.5	348.9
2015	357.2	359.3
2016	5.1	6.1

Table 3 (Continued.)

Year	Start [DOY]	End [DOY]
2016	18.9	21.5
2016	47.1	47.9
2016	66.2	67.2
2016	71.2	71.8
2016	74.7	75.0
2016	86.6	88.1
2016	103.3	104.3
2016	111.8	113.1
2016	113.4	115.1
2016	122.2	124.0
2016	129.0	129.7
2016	135.9	137.0
2016	148.4	149.2
2016	157.3	157.9
2016	162.4	165.2
2016	166.6	167.2
2016	174.4	175.7
2016	188.8	191.1
2016	195.4	196.0
2016	202.0	202.3
2016	210.6	211.3
2016	215.5	216.6
2016	221.3	222.6
2016	236.8	237.5
2016	245.0	246.2
2016	263.8	264.2
2016	268.6	272.0
2016	287.2	288.7
2016	299.3	299.8
2016	315.5	317.4
2016	329.1	330.3
2016	342.5	343.7
2016	355.0	357.1
2017	3.3	5.9
2017	18.0	18.7
2017	26.2	27.3
2017	31.1	31.7
2017	35.8	37.5
2017	60.3	60.9
2017	80.0	80.4
2017	86.0	86.9
2017	97.7	98.6
2017	108.6	110.5
2017	135.3	135.9

Table 3 (Continued.)

Year	Start [DOY]	End [DOY]
2017	138.1	139.3
2017	162.5	162.8
2017	167.1	167.7
2017	175.9	176.7
2017	201.2	202.5
2017	215.5	216.6
2017	223.2	224.8
2017	228.1	229.9
2017	243.2	243.5
2017	257.5	257.8
2017	270.0	271.4
2017	283.8	285.2
2017	297.4	298.4
2017	311.1	312.1
2017	319.2	320.4
2017	324.6	325.5
2017	338.7	339.9
2017	345.2	346.3
2017	350.9	351.7
2017	358.1	358.9
2018	8.3	9.1
2018	13.7	14.4
2018	21.1	22.4
2018	47.0	48.1
2018	53.2	54.9
2018	58.0	58.6
2018	77.3	78.1
2018	99.1	100.4
2018	110.0	110.9
2018	125.4	126.1
2018	142.6	143.6
2018	151.6	152.6
2018	168.6	169.6
2018	177.1	177.2
2018	201.6	202.6
2018	205.2	205.7
2018	227.0	228.5
2018	231.7	232.4
2018	237.6	238.8
2018	253.4	254.6
2018	260.0	260.8
2018	264.7	265.7
2018	274.4	275.0
2018	280.4	280.8

Table 3 (Continued.)

Year	Start [DOY]	End [DOY]
2018	286.3	287.0
2018	308.6	309.8
2018	313.7	314.5
2018	341.2	343.6
2018	361.9	362.7
2019	4.2	5.4
2019	16.7	17.7
2019	23.0	25.1
2019	44.3	44.7
2019	58.4	59.1
2019	87.2	87.6
2019	94.3	94.9
2019	121.2	122.2
2019	146.9	149.5
2019	189.8	190.3
2019	211.4	213.1
2019	217.0	217.9
2019	221.7	222.5
2019	224.2	225.9
2019	238.8	239.6
2019	242.5	243.6
2019	270.3	271.0
2019	273.4	274.6
2019	282.8	283.4
2019	297.3	298.6
2019	324.9	326.1
2019	352.1	353.4

Supplementary Information The online version contains supplementary material available at <https://doi.org/10.1007/s11207-022-01962-1>.

Acknowledgments The work of R. Hajra is funded by the Science and Engineering Research Board (SERB, grant no. SB/S2/RJN-080/2018), a statutory body of the Department of Science and Technology (DST), Government of India through the Ramanujan Fellowship. We would like to thank the reviewer for extremely valuable suggestions that substantially improved the manuscript.

Data Availability The solar-wind plasma and interplanetary magnetic-field data are collected from OMNIWeb (omniweb.gsfc.nasa.gov/). The solar coronal AIA images are taken from NASA's *Solar Dynamics Observatory* (sdo.gsfc.nasa.gov/). The geomagnetic SYM-H and AE indices are obtained from the World Data Center for Geomagnetism, Kyoto, Japan (wdc.kugi.kyoto-u.ac.jp/). The $F_{10.7}$ solar flux are obtained from the LASP Interactive Solar Irradiance Data Center (lasp.colorado.edu/lisird/).

Declarations

Disclosure of Potential Conflicts of Interest The authors declare that there is no conflict of interest.

References

- Allen, R.C., Lario, D., Odstrcil, D., Ho, G.C., Jian, L.K., Cohen, C.M.S., Badman, S.T., Jones, S.I., Arge, C.N., Mays, M.L., Mason, G.M., Bale, S.D., Bonnell, J.W., Case, A.W., Christian, E.R., Dudok de Wit, T., Goetz, K., Harvey, P.R., Henney, C.J., Hill, M.E., Kasper, J.C., Korreck, K.E., Larson, D., Livi, R., MacDowall, R.J., Malaspina, D.M., McComas, D.J., McNutt, R., Mitchell, D.G., Pulupa, M., Raouafi, N., Schwadron, N., Stevens, M.L., Whittlesey, P.L., Wiedenbeck, M.: 2020, Solar wind streams and stream interaction regions observed by the Parker Solar Probe with corresponding observations at 1 au. *Astrophys. J. Suppl.* **246**, 36. [DOI](#).
- Allen, R.C., Ho, G.C., Mason, G.M., Li, G., Jian, L.K., Vines, S.K., Schwadron, N.A., Joyce, C.J., Bale, S.D., Bonnell, J.W., Case, A.W., Christian, E.R., Cohen, C.M.S., Desai, M.I., Filwett, R., Goetz, K., Harvey, P.R., Hill, M.E., Kasper, J.C., Korreck, K.E., Lario, D., Larson, D., Livi, R., MacDowall, R.J., Malaspina, D.M., McComas, D.J., McNutt, R., Mitchell, D.G., Paulson, K.W., Pulupa, M., Raouafi, N., Stevens, M.L., Whittlesey, P.L., Wiedenbeck, M.: 2021, Radial evolution of a CIR: observations from a nearly radially aligned event between Parker Solar Probe and STEREO-A. *Geophys. Res. Lett.* **48**, e2020GL091376. [DOI](#).
- Alves, M.V., Echer, E., Gonzalez, W.D.: 2006, Geoeffectiveness of corotating interaction regions as measured by Dst index. *J. Geophys. Res.* **111**, A07S05. [DOI](#).
- Baker, D.N., Kanekal, S.G., Pulkkinen, T.I., Blake, J.B.: 1999, Equinoctial and solstitial averages of magnetospheric relativistic electrons: a strong semiannual modulation. *Geophys. Res. Lett.* **26**, 3193. [DOI](#).
- Belcher, J.W., Davis, L. Jr.: 1971, Large-amplitude Alfvén waves in the interplanetary medium, 2. *J. Geophys. Res.* **76**, 3534. [DOI](#).
- Boller, B.R., Stolo, H.L.: 1970, Kelvin-Helmholtz instability and the semiannual variation of geomagnetic activity. *J. Geophys. Res.* **75**, 6073. [DOI](#).
- Broun, J.A.: 1848, Observations in magnetism and meteorology made at Makerstoun in Scotland. *Trans. Roy. Soc. Edinb.* **18**, 401.
- Burlaga, L.F., Behannon, K.W., Hansen, S.F., Pneuman, G.W., Feldman, W.C.: 1978, Sources of magnetic fields in recurrent interplanetary streams. *J. Geophys. Res.* **83**, 4177. [DOI](#).
- Burlaga, L.F., Klein, L.W., Lepping, R.P., Behannon, K.W.: 1984, Large-scale interplanetary magnetic fields: Voyager 1 and 2 observations between 1 AU and 9.5 AU. *J. Geophys. Res.* **89**, 10659. [DOI](#).
- Chi, Y., Shen, C., Luo, B., Wang, Y., Xu, M.: 2018, Geoeffectiveness of stream interaction regions from 1995 to 2016. *Space Weather* **16**, 1960. [DOI](#).
- Cliver, E.W., Kamide, Y., Ling, A.G.: 2000, Mountains versus valleys: semiannual variation of geomagnetic activity. *J. Geophys. Res.* **105**, 2413. [DOI](#).
- Cortie, A.L.S.J.: 1912, Sun-spots and terrestrial magnetic phenomena, 1898–1911: the cause of the annual variation in magnetic disturbances. *Mon. Not. Roy. Astron. Soc.* **73**, 52. [DOI](#).
- Daglis, I.A., Thorne, R.M., Baumjohann, W., Orsini, S.: 1999, The terrestrial ring current: origin, formation, and decay. *Rev. Geophys.* **37**, 407. [DOI](#).
- Danilov, A.A., Krymskii, G.F., Makarov, G.A.: 2013, Geomagnetic activity as a reflection of processes in the magnetospheric tail: 1. The source of diurnal and semiannual variations in geomagnetic activity. *Geomagn. Aeron.* **53**, 469. [DOI](#).
- Davis, T.N., Sugiura, M.: 1966, Auroral electrojet activity index AE and its universal time variations. *J. Geophys. Res.* **71**, 785. [DOI](#).
- Dungey, J.W.: 1961, Interplanetary magnetic field and the auroral zones. *Phys. Rev. Lett.* **6**, 47. [DOI](#).
- Echer, E., Tsurutani, B.T., Gonzalez, W.D., Kozyra, J.U.: 2011, High speed stream properties and related geomagnetic activity during the Whole Heliosphere Interval (WHI): 20 March to 16 April 2008. *Solar Phys.* **274**, 303. [DOI](#).
- Frank, L.A.: 1967, On the extraterrestrial ring current during geomagnetic storms. *J. Geophys. Res.* **72**, 3753. [DOI](#).
- Gardner, L., Sojka, J.J., Schunk, R.W., Heelis, R.: 2012, Changes in thermospheric temperature induced by high-speed solar wind streams. *J. Geophys. Res.* **117**, A12303. [DOI](#).
- Gazis, P.R., McDonald, F.B., Burger, R.A., Chalov, S., Decker, R.B., Dwyer, J., Intriligator, D.S., Jokipii, J.R., Lazarus, A.J., Mason, G.M., Pizzo, V.J., Potgieter, M.S., Richardson, I.G., Lanzarotti, L.J.: 1999, Corotating interaction regions in the outer heliosphere. *Space Sci. Rev.* **89**, 269. [DOI](#).
- Gonzalez, W.D., Joselyn, J.A., Kamide, Y., Kroehl, H.W., Rostoker, G., Tsurutani, B.T., Vasyliunas, V.M.: 1994, What is a geomagnetic storm? *J. Geophys. Res.* **99**, 5771. [DOI](#).
- Gopalswamy, N., Nunes, S., Yashiro, S., Howard, R.A.: 2004, Variability of solar eruptions during cycle 23. *Adv. Space Res.* **34**, 391. [DOI](#).
- Gosling, J.T., Hundhausen, A.J., Bame, S.J.: 1976, Solar wind stream evolution at large heliocentric distances: experimental demonstration and the test of a model. *J. Geophys. Res.* **81**, 2111. [DOI](#).

- Grandin, M., Aikio, A.T., Kozlovsky, A.: 2019, Properties and geoeffectiveness of solar wind high-speed streams and stream interaction regions during Solar Cycles 23 and 24. *J. Geophys. Res.* **124**, 3871. DOI.
- Hajra, R.: 2021a, Variation of the interplanetary shocks in the inner heliosphere. *Astrophys. J.* **917**, 91. DOI.
- Hajra, R.: 2021b, Seasonal dependence of the Earth's radiation belt – new insights. *Ann. Geophys.* **39**, 181. DOI.
- Hajra, R.: 2021c, Weakest solar cycle of the space age: a study on solar wind–magnetosphere energy coupling and geomagnetic activity. *Solar Phys.* **296**, 33. DOI.
- Hajra, R., Tsurutani, B.T.: 2018, Chapter 14 – Magnetospheric “killer” relativistic electron dropouts (REDs) and repopulation: a cyclical process. In: Buzulukova, N. (ed.) *Extreme Events in Geospace*, Elsevier, Amsterdam, 373. 978-0-12-812700-1. DOI.
- Hajra, R., Tsurutani, B.T., Lakhina, G.S.: 2020, The complex space weather events of 2017 September. *Astrophys. J.* **899**, 3. DOI.
- Hajra, R., Echer, E., Tsurutani, B.T., Gonzalez, W.D.: 2013, Solar cycle dependence of High-Intensity Long-Duration Continuous AE Activity (HILDCAA) events, relativistic electron predictors? *J. Geophys. Res.* **118**, 5626. DOI.
- Hajra, R., Tsurutani, B.T., Echer, E., Gonzalez, W.D.: 2014a, Relativistic electron acceleration during high-intensity, long-duration, continuous AE activity (HILDCAA) events: solar cycle phase dependences. *Geophys. Res. Lett.* **41**, 1876. DOI.
- Hajra, R., Tsurutani, B.T., Echer, E., Gonzalez, W.D., Brum, C.G.M., Vieira, L.E.A., Santolik, O.: 2015b, Relativistic electron acceleration during HILDCAA events: are precursor CIR magnetic storms important? *Earth Planets Space* **67**, 109. DOI.
- Hajra, R., Tsurutani, B.T., Echer, E., Gonzalez, W.D., Santolik, O.: 2015a, Relativistic ($E > 0.6$, > 2.0 , and > 4.0 MeV) electron acceleration at geosynchronous orbit during high-intensity, long-duration, continuous AE activity (HILDCAA) events. *Astrophys. J.* **799**, 39. DOI.
- Hajra, R., Tsurutani, B.T., Brum, C.G.M., Echer, E.: 2017, High-speed solar wind stream effects on the topside ionosphere over Arecibo: a case study during solar minimum. *Geophys. Res. Lett.* **44**, 7607. DOI.
- Hajra, R., Henri, P., Myllys, M., Héritier, K.L., Galand, M., Simon Wedlund, C., Breuillard, H., Behar, E., Edberg, N.J.T., Goetz, C., Nilsson, H., Eriksson, A.I., Goldstein, R., Tsurutani, B.T., Moré, J., Vallières, X., Wattiaux, G.: 2018, Cometary plasma response to interplanetary corotating interaction regions during 2016 June–September: a quantitative study by the Rosetta Plasma Consortium. *Mon. Not. Roy. Astron. Soc.* **480**, 4544. DOI.
- Hamilton, D.C., Gloeckler, G., Ipavich, F.M., Stüdemann, W., Wilken, B., Kremser, G.: 1988, Ring current development during the great geomagnetic storm of February 1986. *J. Geophys. Res.* **93**, 14343. DOI.
- Hundhausen, A.J., Gosling, J.T.: 1976, Solar wind structure at large heliocentric distances: an interpretation of Pioneer 10 observations. *J. Geophys. Res.* **81**, 1436. DOI.
- Illing, R.M.E., Hundhausen, A.J.: 1986, Disruption of a coronal streamer by an eruptive prominence and coronal mass ejection. *J. Geophys. Res.* **91**, 10951. DOI.
- Iyemori, T., Takeda, M., Nose, M., Odagi, Y., Toh, H.: 2010, Mid-latitude Geomagnetic Indices ASY and SYM for 2009 (Provisional). wdc.kugi.kyoto-u.ac.jp/aeasy/asy.pdf.
- Jian, L.: 2008, PhD thesis, Univ. California Los Angeles.
- Jian, L., Russell, C.T., Luhmann, J.G., Skoug, R.M.: 2006, Properties of stream interactions at one AU during 1995–2004. *Solar Phys.* **239**, 337. DOI.
- Jian, L.K., Russell, C.T., Luhmann, J.G., Skoug, R.M.: 2008b, Evolution of solar wind structures from 0.72 to 1 AU. *Adv. Space Res.* **41**, 259. DOI.
- Jian, L.K., Russell, C.T., Luhmann, J.G., Skoug, R.M., Steinberg, J.T.: 2008a, Stream interactions and interplanetary coronal mass ejections at 0.72 AU. *Solar Phys.* **249**, 85. DOI.
- Jian, L.K., Russell, C.T., Luhmann, J.G., MacNeice, P.J., Odstreil, D., Riley, P., Linker, J.A., Skoug, R.M., Steinberg, J.T.: 2011, Comparison of observations at ACE and *Ulysses* with Enlil model results: stream interaction regions during carrington rotations 2016–2018. *Solar Phys.* **273**, 179. DOI.
- Jian, L.K., Luhmann, J.G., Russell, C.T., Galvin, A.B.: 2019, Solar Terrestrial Relations Observatory (STEREO) observations of stream interaction regions in 2007–2016: relationship with heliospheric current sheets, solar cycle variations, and dual observations. *Solar Phys.* **294**, 31. DOI.
- Kanekal, S.G., Baker, D.N., McPherron, R.L.: 2010, On the seasonal dependence of relativistic electron fluxes. *Ann. Geophys.* **28**, 1101. DOI.
- Krieger, A.S., Timothy, A.F., Roelof, E.C.: 1973, A coronal hole and its identification as the source of a high velocity solar wind stream. *Solar Phys.* **29**, 505. DOI.
- Lei, J., Thayer, J.P., Wang, W., McPherron, R.L.: 2011, Impact of CIR storms on thermosphere density variability during the solar minimum of 2008. *Solar Phys.* **274**, 427. DOI.

- Lockwood, M., Owens, M.J., Barnard, L.A., Haines, C., Scott, C.J., McWilliams, K.A., Coxon, J.C.: 2020, Semi-annual, annual and Universal Time variations in the magnetosphere and in geomagnetic activity: 1. Geomagnetic data. *J. Space Weather Space Clim.* **10**, 23. DOI.
- Marques de Souza Franco, A., Hajra, R., Echer, E., Bolzan, M.J.A.: 2021, Seasonal features of geomagnetic activity: a study on the solar activity dependence. *Ann. Geophys.* **39**, 929. DOI.
- Nakagawa, Y., Nozawa, S., Shinbori, A.: 2019, Relationship between the low-latitude coronal hole area, solar wind velocity, and geomagnetic activity during solar cycles 23 and 24. *Earth Planets Space* **71**, 24. DOI.
- Obridko, V.N., Ivanov, E.V., Özgüç, A., Kilcik, A., Yurchyshyn, V.B.: 2012, Coronal mass ejections and the index of effective solar multipole. *Solar Phys.* **281**, 779. DOI.
- Odrščil, D., Pizzo, V.J.: 1999, Three-dimensional propagation of coronal mass ejections (CMEs) in a structured solar wind flow: 1. CME launched within the streamer belt. *J. Geophys. Res.* **104**, 483. DOI.
- Palmerio, E., Kilpua, E.K.J., Möstl, C., Bothmer, V., James, A.W., Green, L.M., Isavnin, A., Davies, J.A., Harrison, R.A.: 2018, Coronal magnetic structure of earthbound CMEs and in situ comparison. *Space Weather* **16**, 442. DOI.
- Pizzo, V.: 1978, A three-dimensional model of corotating streams in the solar wind, 1. Theoretical foundations. *J. Geophys. Res.* **83**, 5563. DOI.
- Richardson, I.G.: 2018, Solar wind stream interaction regions throughout the heliosphere. *Liv. Rev. Solar Phys.* **15**, 1. DOI.
- Richardson, I.G., Cliver, E.W., Cane, H.V.: 2000, Sources of geomagnetic activity over the solar cycle: relative importance of coronal mass ejections, high-speed streams, and slow solar wind. *J. Geophys. Res.* **105**, 18203. DOI.
- Richardson, I.G., Webb, D.F., Zhang, J., Berdichevsky, D.B., Biesecker, D.A., Kasper, J.C., Kataoka, R., Steinberg, J.T., Thompson, B.J., Wu, C.-C., Zhukov, A.N.: 2006, Major geomagnetic storms ($Dst \leq -100$ nT) generated by corotating interaction regions. *J. Geophys. Res.* **111**, A07S09. DOI.
- Richter, A.K., Luttrell, A.H.: 1986, Superposed epoch analysis of corotating interaction regions at 0.3 and 1.0 AU: a comparative study. *J. Geophys. Res.* **91**, 5873. DOI.
- Russell, C.T., McPherron, R.L.: 1973, Semiannual variation of geomagnetic activity. *J. Geophys. Res.* **78**, 92. DOI.
- Sabine, E.: 1852, VIII. On periodical laws discoverable in the mean effects of the larger magnetic disturbance. No. II. *Phil. Trans. Roy. Soc. London* **142**, 103. DOI.
- Schwabe, H.: 1844, Sonnen-Beobachtungen im Jahre 1843. *Astron. Nachr.* **21**, 233.
- Sheeley, N.R., Harvey, J.W.: 1981, Coronal holes, solar wind streams, and geomagnetic disturbances during 1978 and 1979. *Solar Phys.* **70**, 237. DOI.
- Sheeley, N.R., Asbridge, J.R., Bame, S.J., Harvey, J.W.: 1977, A pictorial comparison of interplanetary magnetic field polarity, solar wind speed, and geomagnetic disturbance index during the sunspot cycle. *Solar Phys.* **52**, 485. DOI.
- Shelley, E.G., Johnson, R.G., Sharp, R.D.: 1972, Satellite observations of energetic heavy ions during a geomagnetic storm. *J. Geophys. Res.* **77**, 6104. DOI.
- Siscoe, G.L.: 1972, Structure and orientations of solar-wind interaction fronts: Pioneer 6. *J. Geophys. Res.* **77**, 27. DOI.
- Smith, E.J., Wolfe, J.H.: 1976, Observations of interaction regions and corotating shocks between one and five AU: Pioneers 10 and 11. *Geophys. Res. Lett.* **3**, 137. DOI.
- Snyder, C.W., Neugebauer, M., Rao, U.R.: 1963, The solar wind velocity and its correlation with cosmic-ray variations and with solar and geomagnetic activity. *J. Geophys. Res.* **68**, 6361. DOI.
- Tanskanen, E.I., Pulkkinen, T.I., Viljanen, A., Mursula, K., Partamies, N., Slavin, J.A.: 2011, From space weather toward space climate time scales: substorm analysis from 1993 to 2008. *J. Geophys. Res.* **116**, A00I34. DOI.
- Tsurutani, B.T., Gonzalez, W.D.: 1987, The cause of high-intensity long-duration continuous AE activity (HILDCAAs): interplanetary Alfvén wave trains. *Planet. Space Sci.* **35**, 405. DOI.
- Tsurutani, B.T., Ho, C.M., Arballo, J.K., Goldstein, B.E., Balogh, A.: 1995, Large amplitude IMF fluctuations in corotating interaction regions: Ulysses at midlatitudes. *Geophys. Res. Lett.* **22**, 3397. DOI.
- Tsurutani, B.T., Gonzalez, W.D., Gonzalez, A.L.C., Guarnieri, F.L., Gopalswamy, N., Grande, M., Kamide, Y., Kasahara, Y., Lu, G., Mann, I., McPherron, R., Soraas, F., Vasyliunas, V.: 2006, Corotating solar wind streams and recurrent geomagnetic activity: a review. *J. Geophys. Res.* **111**, A07S01. DOI.
- Tsurutani, B.T., Hajra, R., Echer, E., Gonzalez, W.D., Santolik, O.: 2016b, Predicting magnetospheric relativistic > 1 MeV electrons. *NASA Tech Briefs* **40**, 20. www.techbriefs.com/component/content/article/ntb/tech-briefs/software/24815.
- Tsurutani, B.T., Hajra, R., Tanimori, T., Takada, A., Remya, B., Mannucci, A.J., Lakhina, G.S., Kozyra, J.U., Shiokawa, K., Lee, L.C., Echer, E., Reddy, R.V., Gonzalez, W.D.: 2016a, Heliospheric plasma sheet (HPS) impingement onto the magnetosphere as a cause of relativistic electron dropouts (REDs)

- via coherent EMIC wave scattering with possible consequences for climate change mechanisms. *J. Geophys. Res.* **121**, 10130. [DOI](#).
- Wang, H., Lühr, H.: 2007, Seasonal-longitudinal variation of substorm occurrence frequency: evidence for ionospheric control. *Geophys. Res. Lett.* **34**, L07104. [DOI](#).
- Wanliss, J.A., Showalter, K.M.: 2006, High-resolution global storm index: Dst versus SYM-H. *J. Geophys. Res.* **111**, A02202. [DOI](#).
- Webb, D.F., Howard, R.A.: 1994, The solar cycle variation of coronal mass ejections and the solar wind mass flux. *J. Geophys. Res.* **99**, 4201. [DOI](#).
- Williams, D.J.: 1987, Ring current and radiation belts. *Rev. Geophys.* **25**, 570. [DOI](#).
- Yurchyshyn, V., Hu, Q., Lepping, R.P., Lynch, B.J., Krall, J.: 2007, Orientations of LASCO Halo CMEs and their connection to the flux rope structure of interplanetary CMEs. *Adv. Space Res.* **40**, 1821. [DOI](#).
- Zhang, Y., Sun, W., Feng, X.S., Deehr, C.S., Fry, C.D., Dryer, M.: 2008, Statistical analysis of corotating interaction regions and their geoeffectiveness during solar cycle 23. *J. Geophys. Res.* **113**, A08106. [DOI](#).

Publisher's Note Springer Nature remains neutral with regard to jurisdictional claims in published maps and institutional affiliations.